



# Design and optimization of the micro-vibration isolation system for large space telescope



Chao Qin <sup>a, b</sup>, Zhenbang Xu <sup>a, c, \*</sup>, Mingyi Xia <sup>a</sup>, Shuai He <sup>a</sup>, Jingxu Zhang <sup>a</sup>

<sup>a</sup> CAS Key Laboratory of On-orbit Manufacturing and Integration for Space Optics System, Changchun Institute of Optics, Fine Mechanics and Physics, Chinese Academy of Sciences

<sup>b</sup> University of Chinese Academy of Sciences, Beijing, 100049, China

<sup>c</sup> Center of Materials Science and Optoelectronics Engineering, University of Chinese Academy of Sciences, Beijing, 100049, China

## ARTICLE INFO

### Article history:

Received 23 July 2019

Received in revised form 27 March 2020

Accepted 14 May 2020

Available online 19 May 2020

Handling Editor: P Tiso

### Keywords:

Large space telescope

Micro-vibration

Vibration isolation system

Line-of-sight

Integrated optomechanical analysis

## ABSTRACT

With increasing demands for better image quality, the aperture and size of a space telescope are becoming larger, and stability requirements are becoming more stringent. To reduce the influence of micro-vibrations on image quality from telescope platform, isolating vibrations of the whole telescope optical payload must be taken into account. To this end, a method to design and optimize a vibration isolation system (VIS) was developed. A dynamic model coupling the telescope optical payload and the platform in orbit was established to assist in the design and optimization of a configuration for the VIS, the objective being to minimize the frequency bandwidth of the integral modes of the telescope optical payload. Isolators with multidirectional elasticity were designed, and the frequency bandwidth of the integral modes was further narrowed by optimizing the structural parameters of the isolators. A viscous fluid damper was designed to suppress the VIS's resonance modes and its damping coefficients tested. Moreover, a micro-vibration integrated optomechanical analysis model was established. The influence of micro-vibration on line-of-sight of a space telescope with VIS was analyzed. The simulation results in the time and frequency domain show that the designed VIS can effectively attenuate the micro-vibrations transmitted to the telescope optical payload.

© 2020 Elsevier Ltd. All rights reserved.

## 1. Introduction

In recent years, high-precision space remote sensing satellites, especially those with large aperture space telescopes, have become a focus of space technology around the world. As technology advances, the image quality of space telescopes is getting higher. However, micro-vibrations can greatly reduce image quality [1]. Micro-vibrations usually have characteristics of low amplitude and wide frequency bandwidth [2]. Depending on the position of installation, the sources of these vibrations in a space telescope fall into two categories: internal disturbance sources of the optical payload and the disturbance sources of the platform. The typical disturbance sources of the former are cryocoolers and mobile mirrors; those of the latter are the reaction flywheel assembly (RWA), solar-array drive mechanisms, and control moment gyroscope (CMG) [3–6]. Comparing

\* Corresponding author. CAS Key Laboratory of On-orbit Manufacturing and Integration for Space Optics System, Changchun Institute of Optics, Fine Mechanics and Physics, Chinese Academy of Sciences, China.

E-mail address: [xuzhenbang@ciomp.ac.cn](mailto:xuzhenbang@ciomp.ac.cn) (Z. Xu).

the two types, disturbances from the telescope platform have larger amplitudes and wider frequency bandwidths. Therefore, they are the principle focus of micro-vibration suppression.

There are three main methods to suppress micro-vibrations in telescope platform are: suppression of sources from for example the RWA and the CMG, optimization of micro-vibration transmission through the spacecraft structure, and vibration isolation for the whole telescope optical payload [7–11]. To meet the strict requirement of micro-vibrations, a variety of methods should be adopted synthetically. The dual-stage vibration isolation system (VIS) composed of micro-vibration source suppression and vibration isolation for the whole telescope optical payload is the most effective. It is the most widely applied measure to suppress micro-vibrations in large space telescopes, for example, the James Webb Space Telescope (JWST), a large-aperture space telescope currently under construction [12], the Terrestrial Planet Finder Coronagraph (TPF-C) to be used to detect exo-planets [13], and the Advanced Technology Large-Aperture Space Telescope (ATLAST), planned to perform spectroscopic observations at wavelengths from ultraviolet to infrared [14].

Some Source vibration isolations are limited by the control bandwidth so that the vibration isolation frequency cannot be too low. This restricts further improvement in its effectiveness, such as the isolation of the CMG. For this reason, vibration isolation for the whole telescope optical payload is an effective supplement to vibration isolation of sources. Better results can be achieved by a dual-stage VIS for the whole telescope optical payload can be categorized as either passive, active or active–passive isolation. Passive vibration isolation is structurally simple, has a high reliability, and does not need external energy, but its effectiveness is limited. Active isolation and active–passive isolation work better than passive isolation, especially at low frequencies. However, their structures are more complicated, reliability is lower, and more energy is consumed. These factors restrict their application in the field of micro-vibration. Consequently, the most widely used vibration isolation technologies still employ passive isolation but with the desire to improve the stability of space telescopes, active and active-passive VISs will be sought more and more.

There are three main factors that determine the VIS performance: configuration, local elasticity, and damping. The research on vibration isolation technologies for the whole telescope optical payload should be performed with all three factors in mind.

In regard to the VIS configuration, as micro-vibrations are usually multiaxial, the VIS for an optical payload should have multiple degrees of freedom. In addition, because the size of the telescope optical payload structure is large, multiple isolators are required to support it. The configuration is very important for multiple isolators. At present, many types of VIS configurations have been studied. They include the tower VIS for the JWST and it is composed of four graphite/epoxy tubular beams [12]. Hexapod configurations also have been widely studied because of its advantages of high symmetry, large stiffness, and good mode decoupling. Examples include an ultra-quiet platform designed by Chen et al. [16] and the miniature VIS (MVIS-II) of McMickell et al. [17]. With a hexapod configuration, the Gough–Stewart isolation system (GSIS) is the most widely used. Examples include a cubic hexapod vibration system for spaceborne interferometry missions designed by Taylor et al. [18], and a GSIS for CMG proposed by Zhang et al. [19]. For a VIS with multiple isolators, optimization of the configuration is crucial. There are generally two objectives in the optimization: one is to achieve mode decoupling of vibrations in each direction, so that the vibration in one direction does not affect the others [20], and the other is to narrow the frequency bandwidth of the integral modes [21]. The resonance zone is thereby minimized to improve vibration isolation in high frequency range. Nevertheless, they do not consider the influence on vibration isolation when the masses of telescope optical payload and the platform are close in orbit.

In regard to elasticity of isolators, the elastic elements are the key parts of a vibration isolator. The general form of the elastic components of the vibration isolators are structures of metal [22], polymer materials [23], and composite materials [15]. With the particularity of the space environment and the demand for high reliability, most elastic structures consist of metal materials. The Hubble telescope's flywheel isolators used metal bellows as the elastic structure [24]. JWST's payload VIS has a metallic A-flexure at the end of each beam [12]. Kamesh et al. designed a low frequency flexible space platform consisting of folded continuous beams that are made of metal [10]. The metal structure has the advantage of outstanding linearity and is easy to process.

Concerning damping in a VIS, damping materials are generally viscous fluids, soft viscoelastic damping materials, and magneto-rheological (MR) fluids. The design and calculation of viscous fluid are more complex, nonetheless, their material stability is good and the technology associated with their use is mature with a broad range of applications, such as the D-struct sets developed by Honeywell Inc [25,26]. They used a viscous fluid to produce damping by having it flow through cavities of different cross-sections. To accommodate the small displacement of a micro-vibration, it is necessary to degas the fluid, otherwise meeting the damping performance specifications may not be achievable. Viscoelastic materials are relatively simple to apply; for instance, a beam was covered with a layer of soft viscoelastic damping material to dissipate the vibrational energy of the JWST [15]. Yet, such materials require high environmental adaptability. In addition, some researchers use a MR fluid to produce damping; for example, Oh et al. designed a MR fluid damper for vibration suppression of a space flexible structure [27].

For the general VIS design, the input and output amplitude–frequency characteristic curves of the VIS are used to evaluate vibration isolation performance. However, for micro-vibration suppression of a space telescope, the influence on image quality is of more concern. Therefore, a complete micro-vibration integrated optomechanical analysis system is needed to assess the effect of VIS. There has been some research, such as the integrated optomechanical analysis based on a finite-element method (FEM) designed by Yang et al. [20], an integrated modeling approach to predict the line-of-sight (LOS) of

the Solar Dynamic Observatory by Liu et al. [28], the multidisciplinary integrated modeling and analysis of space telescopes of Miller et al. [29], and the structural-thermal-optical-analysis for the JWST [30].

In this paper, a method of design and optimization of the VIS for a large aperture space telescope optical payload is studied. The vibration isolation effect is improved by designing and optimizing the configuration of the VIS, and the stiffness and damping of a single vibration isolator synthetically. In Section 2, the structural model of the space telescope is presented. In Section 3, the dynamic model of the coupled system of the telescope optical payload and the platform in orbit was deduced. The mass properties of the optical payload and the platform were both considered. Based on the design of the configuration, the isolators of the VIS with multidirectional elasticity were designed, and the structural parameters of the isolators were optimized. To improve the damping capacity and suppress resonances of the VIS, a viscous fluid damper was designed and its damping coefficients tested. In Section 4, a micro-vibration integrated analysis model was established. The influence of micro-vibrations on the LOS of the space telescope with the optimized VIS was analyzed. From simulation results in the time and frequency domains, we verified the performance of the VIS.

## 2. Structural model of the space telescope

The model of the space telescope (Fig. 1) consists of two main parts: the telescope optical payload and the telescope platform. The aperture of the telescope is 1 m and its mass is 2.7 t. The telescope optical payload uses a Cassegrain optical system, including a parabolic primary mirror and a hyperbolic secondary mirror. The telescope platform is composed of carbon-fiber frames and solar arrays.

The VIS is located between the optical payload and telescope platform. The Gough–Stewart configuration is adopted for the VIS and includes a payload platform, a base platform, and six isolators. The payload platform is at the bottom of the telescope optical payload and the base platform is at the top of the telescope platform. Each isolator consists of an elastic structure and a damping structure arranged in parallel.

## 3. Design and optimization of the VIS

The main micro-vibration sources are the momentum wheel assemblies that are located in the telescope platform (Fig. 1). Therefore, the VIS between telescope optical payload and the platform is the main object of this study. Once the basic frequency of the VIS is known, the effect of the VIS can be determined and essentially depend on the frequency bandwidth of the integral modes of the telescope optical payload and VIS damping characteristics. To narrow the frequency bandwidth down, the configuration of VIS and the elastic structure of single isolator were designed and optimized. For damping, a viscous fluid damper was tested and applied in VIS simulations. The design and optimization flow is shown in Fig. 2.

### 3.1. Design and optimization of the configuration of VIS

The VIS has a Gough–Stewart configuration. The coordinates and symbols definitions of the VIS are shown in Fig. 3  $\{P\}$  and  $\{B\}$  denote the coordinate frames for the payload platform and the base platform;  $\{O\}$  denotes the basic coordinate frame. In the initial state,  $\{B\}$  and  $\{O\}$  coincide. The vector  ${}^O\Phi_P = [{}^O\mathbf{t}_P, {}^O\mathbf{q}_P]$  denotes the pose of the payload platform relative to  $\{O\}$  in which vector  ${}^O\mathbf{t}_P$  denotes the position of the origin P of  $\{P\}$  in  $\{O\}$ , vector  ${}^O\mathbf{q}_P = [{}^O\gamma_P, {}^O\alpha_P, {}^O\beta_P]^T$  denotes the posture of the payload platform relative to  $\{O\}$ . In the same manner,  ${}^O\Phi_B = [{}^O\mathbf{t}_B, {}^O\mathbf{q}_B]$  is defined.  ${}^P\mathbf{p}_i$  denotes the joint points of the payload platform in  $\{P\}$ ,  ${}^B\mathbf{b}_i$  denotes the joint points of the base platform in  $\{B\}$ .  $R_P$  and  $R_B$  represent the radii of the payload platform and base platform, respectively. The angle between  $P_4$  and  $P_5$  is  $\phi$ ; the angle between  $B_1$  and  $B_6$  is  $\theta$ .

The traditional VIS design is premised on the base platform being fixed and the optical payload is the movable mass. However, in reality, a large space telescope in orbit is free-free, both ends of the VIS are unconstrained masses. The differences between the assumptions of the two setups are illustrated in Fig. 4. In this study, the masses of both the telescope optical payload and the platform are considered when the VIS is designed.

First, the natural frequencies of the VIS are deduced. For rod  $B_iP_i$  in the basic coordinate  $\{O\}$ , denoted by  ${}^O\mathbf{l}_i$ , we obtain

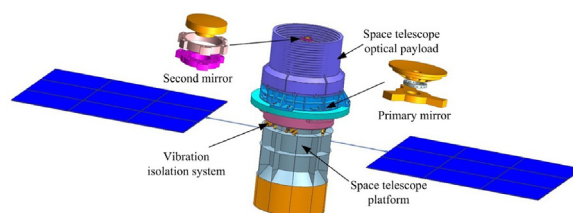


Fig. 1. Structural model of the space telescope.

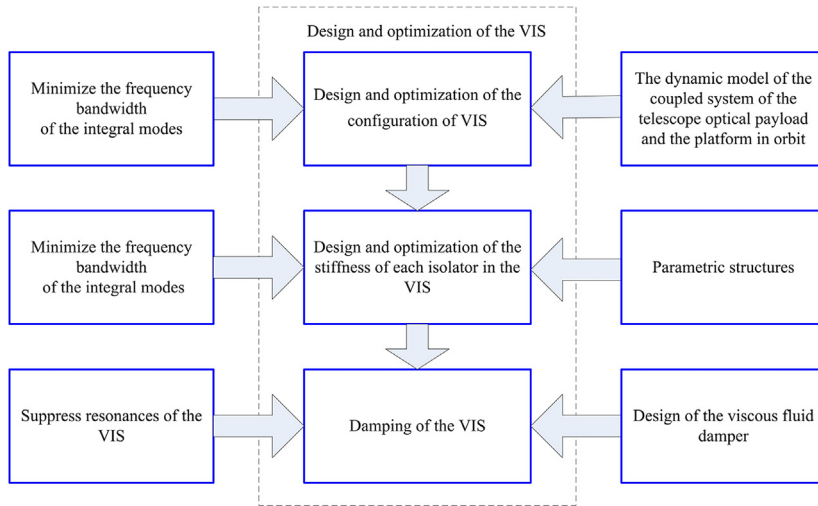


Fig. 2. Design and optimization flow diagram.

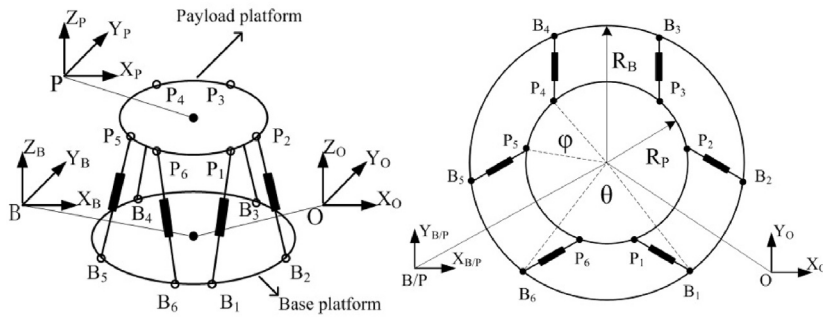


Fig. 3. Definitions of coordinates and symbols of the VIS structure.

$${}^O \mathbf{l}_i = {}^O \mathbf{t}_P + {}^O \mathbf{R} \cdot {}^P \mathbf{p}_i - ({}^O \mathbf{t}_B + {}^O \mathbf{R} \cdot {}^B \mathbf{b}_i), \tag{1}$$

where  $\mathbf{R}$  is the rotation matrix. The rod length is  $l_i = \sqrt{{}^O \mathbf{I}_i^T \cdot {}^O \mathbf{I}_i}$ . Let  ${}^O \mathbf{l}_{ni}$  denote the unit vector in  $\{O\}$ ,  ${}^O \mathbf{l}_{ni} = {}^O \mathbf{I}_i / l_i$ . The velocities of the joint points of the payload platform and base platform are respectively

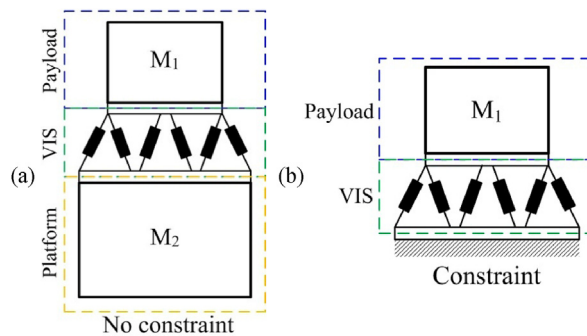


Fig. 4. Differences between the two boundary conditions: (a) mass of telescope platform is considered; (b) the mass of telescope platform is constraint.

$${}^0\mathbf{v}_{Pi} = {}^0\dot{\mathbf{t}}_p + {}^0\boldsymbol{\omega}_i \times {}^0_P\mathbf{R} \cdot {}^P\mathbf{p}_i, \quad (2)$$

$${}^0\mathbf{v}_{Bi} = {}^0\dot{\mathbf{t}}_B + {}^0\boldsymbol{\omega}_B \times {}^0_B\mathbf{R} \cdot {}^B\mathbf{b}_i. \quad (3)$$

The expansion rate of rod is

$$\dot{l}_i = {}^0\mathbf{I}_{ni}^T \cdot ({}^0\mathbf{v}_{Pi} - {}^0\mathbf{v}_{Bi}). \quad (4)$$

Hence, substituting Eqs. (2) and (3) into Eq. (4) gives

$$\dot{l}_i = \begin{bmatrix} {}^0\mathbf{I}_{ni}^T, -{}^0\mathbf{I}_{ni}^T, ({}^0_P\mathbf{R} \cdot {}^P\mathbf{p}_i \times {}^0\mathbf{I}_{ni})^T, -({}^0_B\mathbf{R} \cdot {}^B\mathbf{b}_i \times {}^0\mathbf{I}_{ni})^T \end{bmatrix} \begin{bmatrix} {}^0\dot{\mathbf{t}}_p \\ {}^0\dot{\mathbf{t}}_B \\ {}^0\boldsymbol{\omega}_p \\ {}^0\boldsymbol{\omega}_B \end{bmatrix}. \quad (5)$$

The matrix of the unit vectors of all rods  ${}^0\mathbf{L}_n$ , is defined as

$${}^0\mathbf{L}_n = [{}^0\mathbf{l}_{n1}, {}^0\mathbf{l}_{n2}, {}^0\mathbf{l}_{n3}, {}^0\mathbf{l}_{n4}, {}^0\mathbf{l}_{n5}, {}^0\mathbf{l}_{n6}]. \quad (6)$$

The Jacobian matrix of the velocities to the expansion rates of the rods is defined as

$$\mathbf{J} = [{}^0\mathbf{L}_n^T, -{}^0\mathbf{L}_n^T, ({}^0_P\mathbf{R} \cdot {}^P\mathbf{P} \times {}^0\mathbf{L}_n)^T, -({}^0_B\mathbf{R} \cdot {}^B\mathbf{B} \times {}^0\mathbf{L}_n)^T], \quad (7)$$

where  ${}^P\mathbf{P}$  and  ${}^B\mathbf{B}$  are the coordinate matrices of the point locations of the joints of the payload and base platforms, respectively.

The generalized stiffness matrix  $\mathbf{K}$  of the VIS is

$$\mathbf{K} = k \cdot \mathbf{J}^T \mathbf{J}, \quad (8)$$

and the generalized mass matrix  $\mathbf{M}$  of the VIS is

$$\mathbf{M} = \begin{bmatrix} m_p \mathbf{E}_3 & \mathbf{O}_3 & m_p {}^0_P\mathbf{R} \cdot {}^P\mathbf{C}_p^T \cdot {}^0_P\mathbf{R}^T & \mathbf{O}_3 \\ \mathbf{O}_3 & m_B \mathbf{E}_3 & \mathbf{O}_3 & m_B {}^0_B\mathbf{R} \cdot {}^B\mathbf{C}_B^T \cdot {}^0_B\mathbf{R}^T \\ m_p {}^0_P\mathbf{R} \cdot {}^P\mathbf{C}_p \cdot {}^0_P\mathbf{R}^T & \mathbf{O}_3 & {}^0\mathbf{I}_p & \mathbf{O}_3 \\ \mathbf{O}_3 & m_B {}^0_B\mathbf{R} \cdot {}^B\mathbf{C}_B \cdot {}^0_B\mathbf{R}^T & \mathbf{O}_3 & {}^0\mathbf{I}_B \end{bmatrix}, \quad (9)$$

where  $\mathbf{E}_3$  is the  $3 \times 3$  identity matrix,  $\mathbf{O}_3$  the  $3 \times 3$  zero matrix,  $m_p$  and  $m_B$  are the masses of the telescope optical payload and telescope platform, respectively,  $\mathbf{C}$  denotes a skew symmetry matrix obtained from the spatial vector of the centroid, and  $\mathbf{I}$  is the inertia matrix.

The free vibration equation of the VIS without damping is

$$\mathbf{M}\ddot{\boldsymbol{\Phi}} + \mathbf{K}\boldsymbol{\Phi} = \mathbf{0}. \quad (10)$$

By solving the characteristic equation corresponding to the ordinary differential Eq. (10), the first 12 natural frequencies of the VIS can be obtained; the 1st to 6th correspond to free modes, whereas the 7th to the 12th correspond to integral modes of the space telescope.

The parameters needing to be determined for the configuration are  $R_p$  and  $R_B$ ,  $H$  (the height of the VIS),  $\theta$  (or  $\phi$ ,  $\theta + \phi = 120^\circ$ ), and  $k$  (the stiffness of an isolator); they are listed in Table 1. Because of design constraints,  $R_p$  and  $R_B$  have specific values.

In the optimization process,  $H$ ,  $\theta$  and  $k$  are set to their optimized values while solving the characteristic equation, Eq. (10). The downhill-simple and genetic algorithms in the optimization toolbox were combined for optimizing. The objective was to minimize the ratio between the frequencies of mode 12th and mode 7th, and consider the requirement of control bandwidth, constraint condition of mode 7th is  $5 \text{ Hz} \pm 1 \text{ Hz}$ , the optimization function is defined as

**Table 1**  
Parameter settings of the VIS.

$R_P$	$R_B$	Height of VIS, $H$	$\theta$	Stiffness of isolator, $k$
0.45 m	0.5 m	Undetermined	Undetermined	Undetermined

$$\min \left\{ \text{Target} = \frac{f_{12th}(H, \theta, k)}{f_{7th}(H, \theta, k)} \right\}. \quad (11)$$

The results of the optimization are listed in Table 2.

Using these optimized parameter settings, a comparison of results for the six integral modes of the VIS using the FEM was obtained (Table 3). The FE model corresponds to the telescope structure mentioned in section 2, the details are shown in section 4.1.1. The maximum deviation is 3.09% with the main deviation sources coming from the flexibility of the platform connections and the simplified treatment of these connections in the FEM. The results show that the formulas derived above may be used to calculate the natural frequencies of the VIS.

To illustrate the optimization effect, the frequencies of the cubic configuration of the VIS at same fundamental frequency are calculated by FEM (Table 4). The frequency ratio of the optimized VIS above is 2.04 and that of the cubic configuration is 2.79. The former is clearly smaller than the latter.

With each isolator of the VIS having the same axial stiffness, the optimized VIS with a minimum bandwidth for the six integral modes is obtained. The free-free state of the telescope and the mass of the telescope platform are both taken into account.

### 3.2. Design and optimization of the stiffness of each isolator in the VIS

#### 3.2.1. Optimization of the stiffness of each isolator

In the configuration optimization process of the VIS above, it is assumed that the stiffness of each isolator is the same, and the entire VIS is a symmetric structure with regard to stiffness. However, both the telescope optical payload and the platform have mass eccentricities. To improve further the effect of the VIS, six isolators with different stiffness are considered in the design, each having a local stiffness that is designed for each of three orthogonal directions. Thus, the structure of a single isolator (Fig. 5) has three flexible parts with adjustable thicknesses. Hence the total number of parameters for the six isolators is 18. The configuration of the VIS in this section is the same with the optimized one in Section 3.1.

The VIS including the isolators of the space telescope was configured as a finite-element model (FE model), taking the 18 adjustable thicknesses as optimization variables. In applying both the downhill-simple and genetic algorithms in the optimization, running on the integrated FEM software programs, MSC Nastran and MATLAB, the optimized parameters can be got. We used the optimization function,

**Table 2**  
Optimized parameter settings of the VIS.

$R_P$	$R_B$	Height of VIS, $H$	$\theta$	Stiffness of isolator, $k$
0.45 m	0.5 m	0.11 m	67.6°	676,650 N/m

**Table 3**  
Natural frequencies of VIS with optimized parameter settings.

Mode	1st–6th (Hz)	7th (Hz)	8th (Hz)	9th (Hz)	10th (Hz)	11th (Hz)	12th (Hz)	$\frac{f_{12th}}{f_{7th}}$
Formula	0	5.01	5.01	6.09	9.68	9.76	10.21	2.04
FEM	0	4.86	4.92	5.94	9.48	9.53	10.01	2.06
Deviation	–	3.09%	1.83%	2.53%	2.11%	2.41%	2.00%	–

**Table 4**  
Comparison of the cubic configuration and optimized VIS with the same fundamental frequency.

Mode	1st–6th (Hz)	7th (Hz)	8th (Hz)	9th (Hz)	10th (Hz)	11th (Hz)	12th (Hz)	$\frac{f_{12th}}{f_{7th}}$
Optimized VIS	0	5.01	5.01	6.09	9.68	9.76	10.21	2.04
Cubic	0	5.03	5.05	8.11	9.99	13.97	14.03	2.79

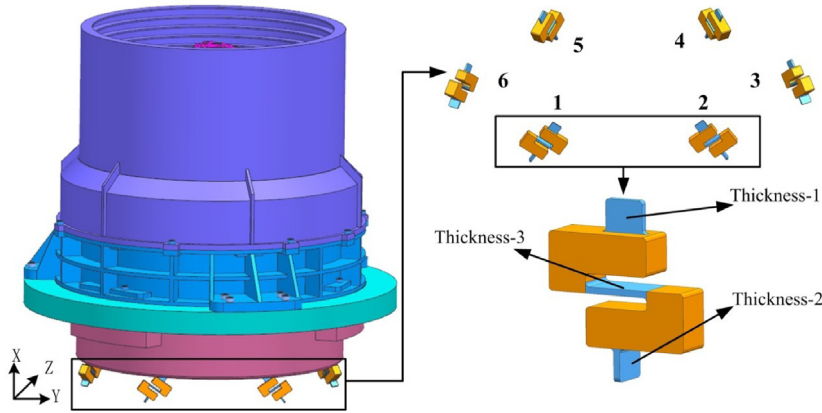


Fig. 5. Structure of the six isolators.

$$\min \left\{ \text{Target} = \frac{f_{12th}(t_{11}, t_{12}, \dots, t_{ij}, \dots, t_{63})}{f_{7th}(t_{11}, t_{12}, \dots, t_{ij}, \dots, t_{63})} \right\}, \tag{12}$$

where  $f$  is the natural frequency of the VIS, and  $t_{ij}$  the adjustable thicknesses of the isolators,  $i = 1-6$  indexes the isolators, and  $j = 1-3$  the thicknesses of the corresponding isolator. The optimized results are listed in Table 5.

We introduced the above parameter settings into the FE model of the space telescope. The natural frequencies of the six integral modes, pre- and post-optimization of stiffness, are listed in Table 6. Without stiffness optimization, the state is that described in Section 3.1 in which each isolator only has axial stiffness and the stiffness of the six isolators are the same. The configuration of the VIS in this section is the same as that optimized in Section 3.1. The results in Table 6 show that the frequency bandwidth of the six integral modes is reduced from 5.15 Hz to 2.97 Hz, the ratio of the 12th modal frequency to 7th modal frequency is reduced from 2.06 to 1.57.

### 3.2.2. Validation of the stiffness optimization method

In order to verify the optimization method in section 3.2.1, an experiment is designed, the structures of the experimental system are shown in Fig. 6. The experimental system has two states: pre- and post-optimization of stiffness. The upper and base platforms are shared, there are 6 isolators for the VIS without stiffness optimization and another 6 isolators for the VIS with stiffness optimization. The masses of the upper and base platforms are 80.78 kg and 86.45 kg, the material is iron. The isolators' material is aluminum alloy. The parameters of the isolators with and without stiffness optimization are listed in Table 7 and Table 8.

The FE models of the experimental system are established, the modal analysis is completed, the boundary condition is free-free. The results are shown in Fig. 7, mode 1st-6th correspond to free modes. With stiffness optimization, the ratio of mode 12th to mode 7th reduces from 1.86 to 1.33. Then the experimental verification is carried out.

Table 5  
Optimized results of isolators.

Isolator number	Thickness-1 (mm)	Thickness-2 (mm)	Thickness-3 (mm)
1	9.8	9.5	3
2	9.7	9.6	3.1
3	9.5	8.7	3
4	9.5	9.5	3
5	9.6	9.5	3.1
6	9.5	9.4	3

Table 6  
Natural frequencies of the VIS with and without stiffness optimization.

Mode	1st-6th (Hz)	7th (Hz)	8th (Hz)	9th (Hz)	10th (Hz)	11th (Hz)	12th (Hz)	$\frac{f_{12th}}{f_{7th}}$
Without stiffness optimization	0	4.86	4.92	5.94	9.48	9.53	10.01	2.06
With stiffness optimization	0	5.25	5.25	5.52	7.58	8.21	8.22	1.57

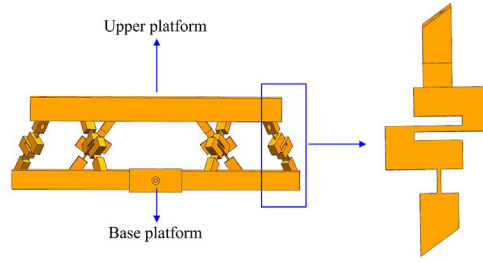


Fig. 6. The structure of the experimental system.

Table 7  
Parameters of isolators without stiffness optimization.

Isolator number	Thickness-1 (mm)	Thickness-2 (mm)	Thickness-3 (mm)
1	2	2	3
2	2	2	3
3	2	2	3
4	2	2	3
5	2	2	3
6	2	2	3

Table 8  
Parameters of isolators with stiffness optimization.

Isolator number	Thickness-1 (mm)	Thickness-2 (mm)	Thickness-3 (mm)
1	3.9	3.0	2.0
2	4.6	2.0	2.4
3	3.4	3.0	2.2
4	4.7	2.6	2.4
5	2.1	2.3	2.4
6	5.0	3.2	2.3

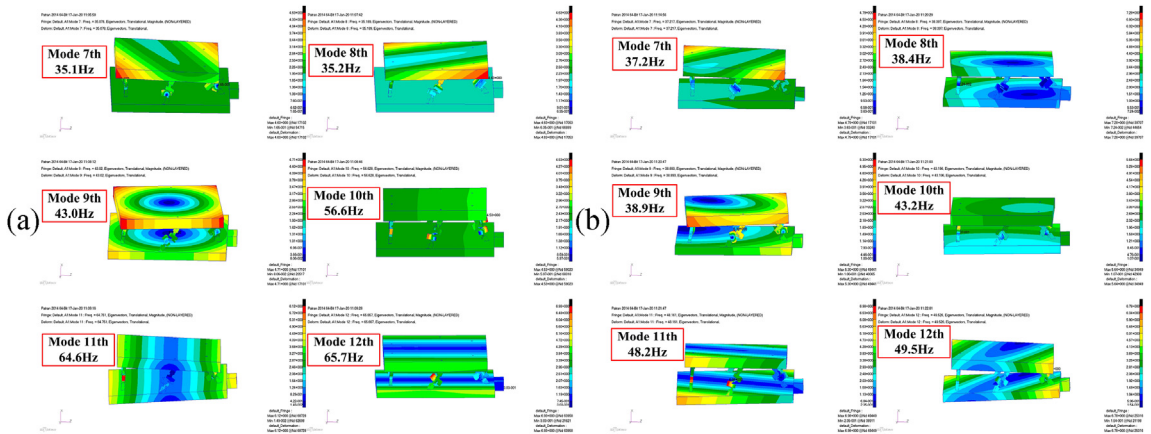


Fig. 7. The FE method results: (a) without stiffness optimization, (b) with stiffness optimization.

The 12 isolators of the two sets of experimental systems are shown in Fig. 8. The whole experimental system is composed of test system, suspension system and the VIS. The excitation form is transient impact, as shown in Fig. 9.

The experimental results are shown in Fig. 10. By comparing the results in Table 9, the maximum deviation is 7.6%, this is due to the simplification of the FE models. The experimental results show that the stiffness optimization method in section 3.2.1 can reduce the frequency bandwidth of the integral modes of the VIS effectively.

Up to this point, the design and optimization of the VIS configuration and the elastic performance of single isolator have been completed. To improve the low-frequency performance of the VIS, an analysis of damping was performed.

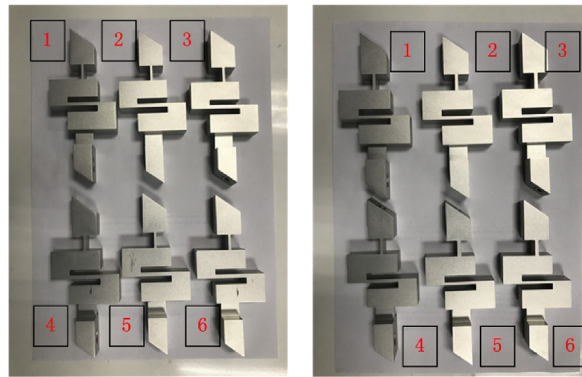


Fig. 8. The photos of isolators.

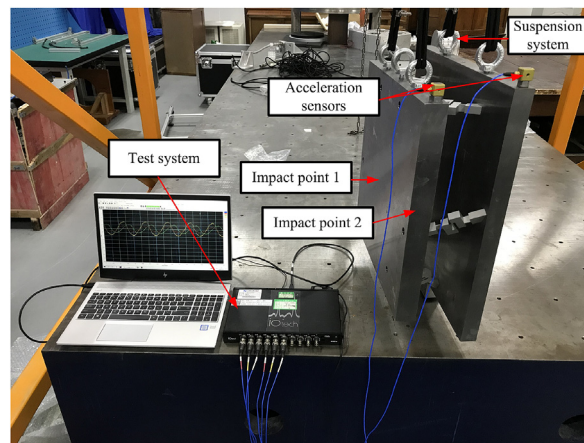


Fig. 9. The experimental system.

### 3.3. Design of the viscous fluid damper

According to vibration isolation theory, the addition of VIS produces resonance at the natural frequencies. The resonance can be reduced by adding damping. For improving the effect, the damping should have the characteristics: high damping in the low frequency range and low damping in the high frequency range. Therefore, viscous fluid dampers are adopted, each isolator equipped with a single damper, and the six sets are shown in Fig. 11(a).

To facilitate the installation, the isolator and damper should be integrated installation. To improve the damping effect, the axis of the damper ought to be installed in the X–Y plane of isolator's local coordinate (Fig. 11(b)). Because when the VIS resonates, the sheet metal in the middle of the isolator is the main deformed part, its deformation is the largest in this plane. That means the relative displacement of both ends of the isolator is the largest in this plane, and the large relative displacement is beneficial for dissipation of vibration energy.

The viscous fluid damper has a clearance-type design (Fig. 12). The clearance through which the damping fluid passes is formed by the axle and the flange. Because the volume of the cavity is constant, when the upper and lower flexible joints vibrate relative to each other, fluid flows between the upper and lower cavities along the clearance and produces damping. The amount of damping is determined by the size of the cavities and the type of damping fluid. Both ends of the damper are designed with flexible joints to reduce the additional stiffness and the leaf springs also have the same function.

The most common method to test the damping of the viscous fluid damper is the hysteresis loop method (Fig. 13). Because of axial stiffness, the test hysteresis loop is oriented at angle  $\theta$  to the horizontal axis; the stiffness is related to the angle by

$$k = \tan(\theta). \quad (13)$$

Because the elastic force generated by the axial stiffness does not expend energy, the equivalent damping coefficient  $c$  is expressed as

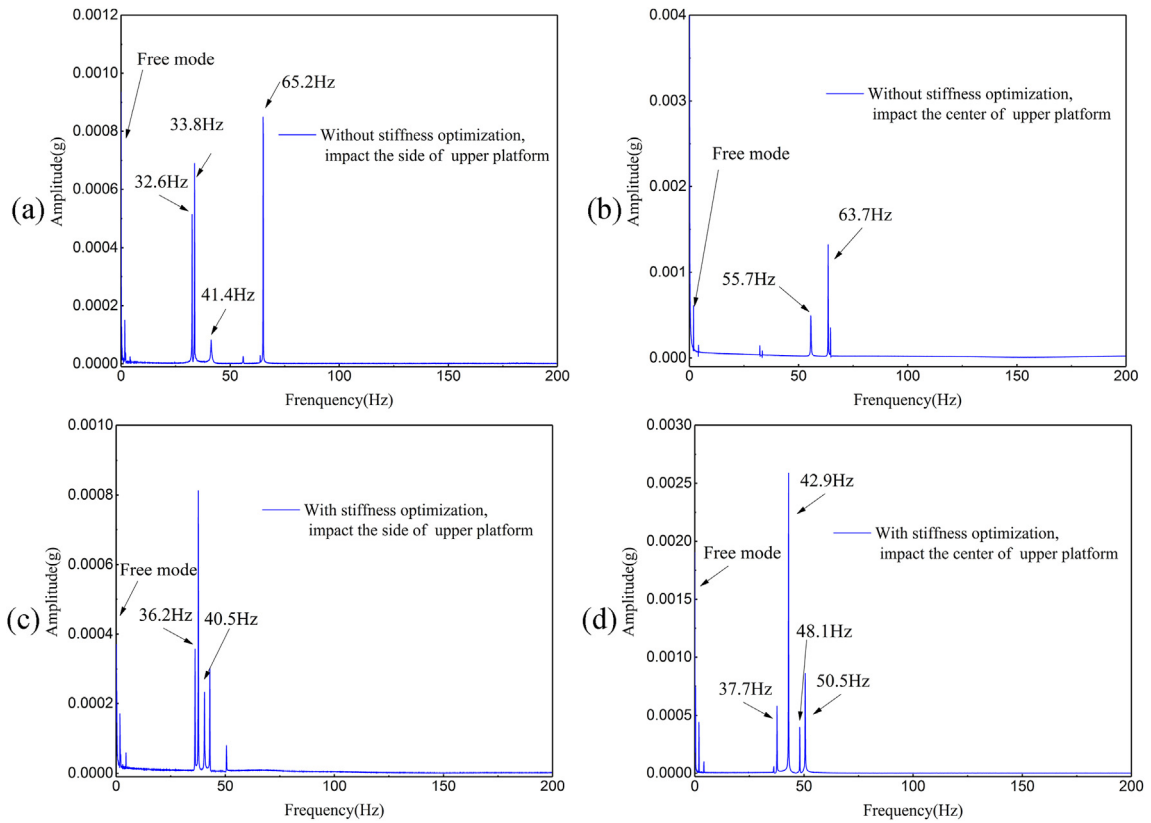


**Fig. 10.** The experimental results: (a) and (b) are frequency distributions without stiffness optimization, (c) and (d) are frequency distributions with stiffness optimization.

**Table 9**  
Comparison of the FE-method and experimental results.

Result	State	Mode 7th (Hz)	Mode 8th (Hz)	Mode 9th (Hz)	Mode 10th (Hz)	Mode 11th (Hz)	Mode 12th (Hz)	$\frac{f_{12th}}{f_{7th}}$
The FE-method results	Without stiffness optimization	35.1	35.2	43.0	56.6	64.6	65.7	1.87
	With stiffness optimization	37.2	38.4	38.9	43.2	48.2	49.5	1.33
The experimental results	Without stiffness optimization	32.6	33.8	41.4	55.7	63.7	65.2	2.00
	With stiffness optimization	36.2	37.7	40.5	42.9	48.1	50.5	1.39

\*Mode1st-6th are free modes.

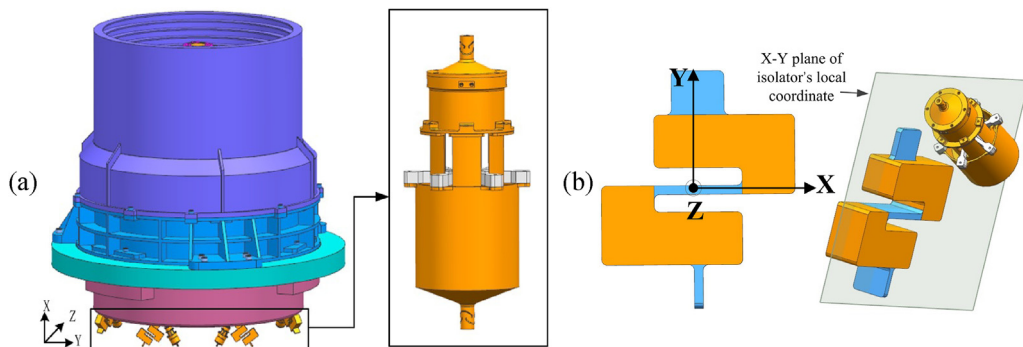


**Fig. 11.** Installation form of the viscous fluid dampers.

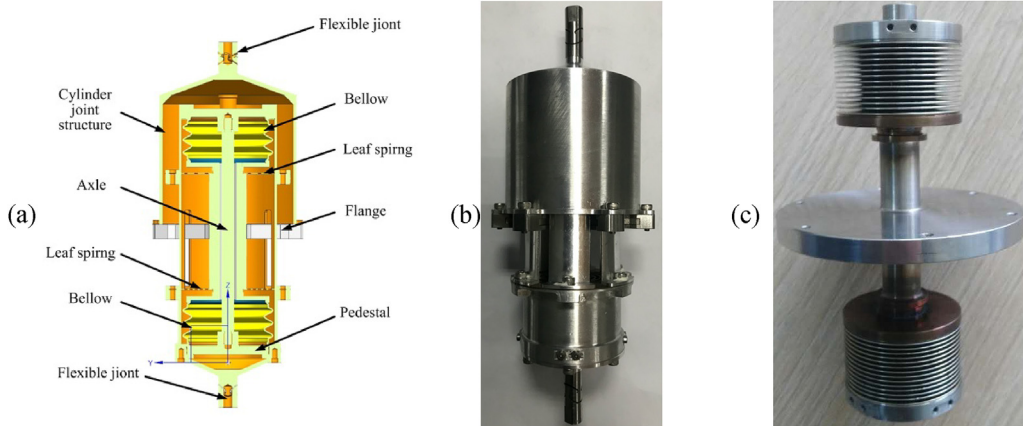


Fig. 12. Structure of the viscous fluid damper: (a) cross-sectional structure, and photos of (b) the damper, and (c) the bellows.

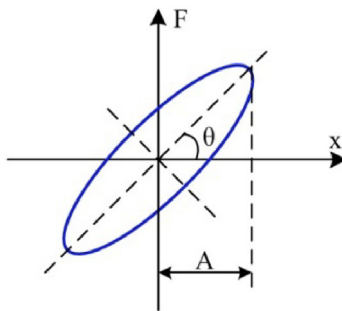


Fig. 13. Schematic diagram of the hysteresis loop obtained from the damping test. The axial force ( $F$ )–displacement ( $x$ ) curve traces out a hysteresis loop.

$$c = \frac{S}{\pi\omega A^2}. \tag{14}$$

where  $A$  is the amplitude of the displacement and  $S$  is the area of the ellipse [31].

The test system (Fig. 14) comprises a force sensor, laser displacement sensor, vibration exciter, and data collection and analysis system. In the damping test, the exciter outputs a sinusoidal disturbance, given by its control system, through the series force sensor (PCB–208C03, resolution: 0.02 N-rms, sensitivity: 2.248 mV/N, range: 2.224 kN) to the flexible joint on the top of the damper. The displacement at the other end of the damper is measured by a non-contact laser displacement sensor (optoNCDT-2300LL, resolution: 0.03  $\mu\text{m}$ -20 kHz, absolute error:  $\leq \pm 0.03\%$ FS, range: 2 mm). During testing, the force signal and

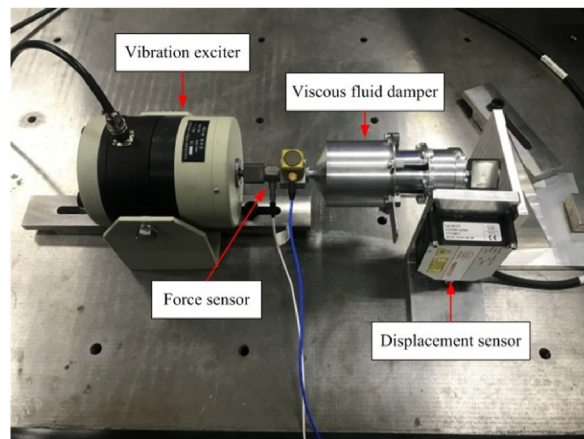


Fig. 14. Test system for analyzing the damper using the hysteresis loop method.

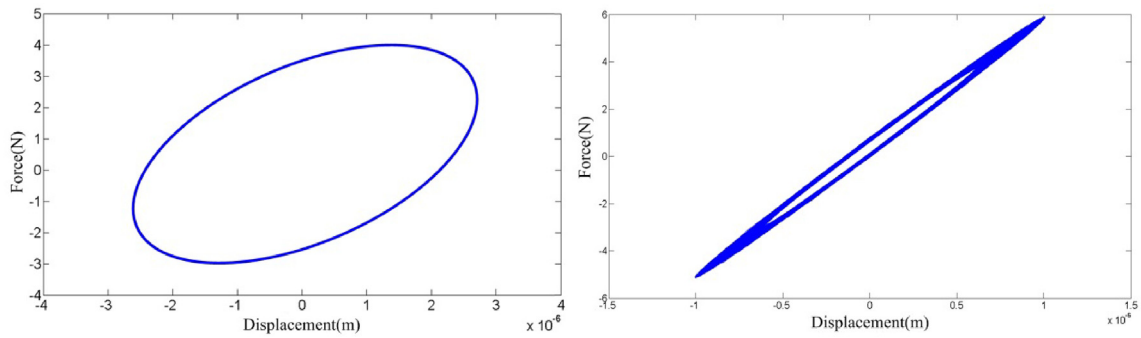


Fig. 15. Typical hysteresis loops obtained for low and high frequencies.

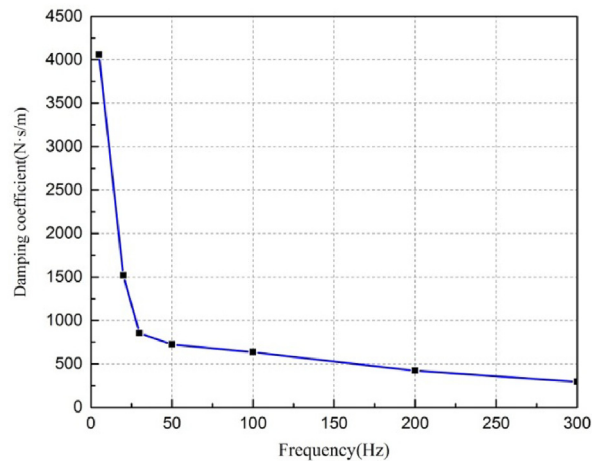


Fig. 16. Dependence of the damping coefficient on excitation frequency obtained in tests.

displacement signal are processed by the data collection and analysis system. For given frequency, the hysteresis loops between force and displacement are produced during data processing. After adjusting the excitation frequency, the above steps are repeated to obtain a hysteresis loop for each frequency. From the hysteresis loops obtained with low frequency and high frequency excitations (Fig. 15), the damping coefficient clearly changes as the area of the ellipse changes. The values of the equivalent damping coefficient for different frequencies were plotted (Fig. 16).

Fig. 16 showing that as the excitation frequency increases, the damping coefficient decreases significantly, a characteristic of fluid damping. At high frequency, the vibration displacement is small, because of the presence of gas in the fluid that leads to compressibility of the fluid. When a vibration occurs, the fluid in the middle part cannot flow, resulting in a reduction in damping. This phenomenon is more obvious in the relaxation-type fluid damper [32]. The test results of the damper in this study show that the damping coefficients within 20 Hz are greater than 1500 Ns/m.

Thus far, the main factors of the VIS have been designed. We continue the simulation analysis to assess the effect of the VIS.

#### 4. Simulation of the effect of the VIS

The LOS is the main index to evaluate the influence of micro-vibrations on the space telescope. For this study, a micro-vibration integrated optomechanical analysis model, including a disturbance source model, a structural FE model, and an optical model, was established with which we analyzed the effect of the designed VIS on the pointing stability of a space telescope. In this section, the state of the space telescope with and without the above designed VIS is analyzed using this model, and the effects are simulated both in the frequency and time domains.

##### 4.1. Micro-vibration integrated optomechanical analysis model

The integrated analysis model comprises mainly the structural FE model, optical model, and disturbance source model. The three models are integrated to calculate the influence of micro-vibration on the LOS of space telescope.

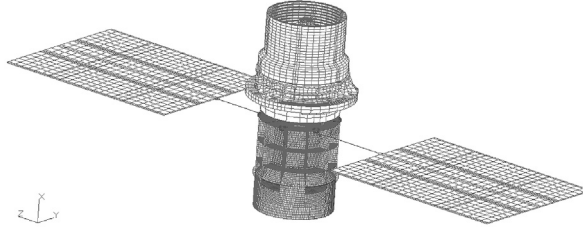


Fig. 17. Structural FE model of the space telescope.

#### 4.1.1. Structural FE model

The structural FE model is established based on the structure of the space telescope (Fig. 17) and is divided into three parts: telescope optical payload, VIS, and telescope platform. The FE models of the main components of the structure are all established. The final FE model includes 72,038 elements and 106,056 nodes.

#### 4.1.2. Optical model

The optical model comprises the fitting equations for the rigid body motion of the mirror and the matrix of the sensitivity coefficients for an image point. For the former, because the mirror surfaces consist of nodes in the FE model, the displacements  $[dx'_i, dy'_i, dz'_i]$  of the node  $(x_i, y_i, z_i)$  on the mirror surface due to the rigid-body displacements  $[T_x, T_y, T_z, R_x, R_y, R_z]$  of the mirror are assumed to be expressed in the form

$$\begin{aligned} dx'_i &= T_x + z_i R_y - y_i R_z \\ dy'_i &= T_y - z_i R_x + x_i R_z \\ dz'_i &= T_z + y_i R_x - x_i R_y. \end{aligned} \quad (15)$$

We define the error  $E$  as the weighted sum of the square of difference between the actual nodal displacements  $[dx_i, dy_i, dz_i]$  and the displacements  $[dx'_i, dy'_i, dz'_i]$  due to rigid-body displacements above,

$$E = \sum_{i=1}^n \omega_i \left[ (dx_i - dx'_i)^2 + (dy_i - dy'_i)^2 + (dz_i - dz'_i)^2 \right]. \quad (16)$$

where  $\omega_i$  is the weight associated with mirror surface node  $i$ .

The best-fit motion of the mirror is given by the minimum of  $E$ , i.e., the partial derivative of  $E$  with respect to  $[T_x, T_y, T_z, R_x, R_y, R_z]$  is equal to zero. Hence, it can be further expressed as

$$\begin{aligned} \sum_{i=1}^n \omega_i T_x + \sum_{i=1}^n \omega_i z_i R_y - \sum_{i=1}^n \omega_i y_i R_z &= \sum_{i=1}^n \omega_i dx_i \\ \sum_{i=1}^n \omega_i T_y - \sum_{i=1}^n \omega_i z_i R_x + \sum_{i=1}^n \omega_i x_i R_z &= \sum_{i=1}^n \omega_i dy_i \\ \sum_{i=1}^n \omega_i T_z + \sum_{i=1}^n \omega_i y_i R_x - \sum_{i=1}^n \omega_i x_i R_y &= \sum_{i=1}^n \omega_i dz_i \\ \sum_{i=1}^n \omega_i z_i T_y - \sum_{i=1}^n \omega_i y_i T_z + \sum_{i=1}^n \omega_i x_i y_i R_y - \sum_{i=1}^n \omega_i (y_i^2 + z_i^2) R_x + \sum_{i=1}^n \omega_i x_i z_i R_z &= \sum_{i=1}^n \omega_i dy_i z_i - \sum_{i=1}^n \omega_i dz_i y_i \\ \sum_{i=1}^n \omega_i z_i T_x - \sum_{i=1}^n \omega_i x_i T_z - \sum_{i=1}^n \omega_i x_i y_i R_x + \sum_{i=1}^n \omega_i (x_i^2 + z_i^2) R_y - \sum_{i=1}^n \omega_i y_i z_i R_z &= \sum_{i=1}^n \omega_i dx_i z_i - \sum_{i=1}^n \omega_i dz_i x_i \\ \sum_{i=1}^n \omega_i y_i T_x - \sum_{i=1}^n \omega_i x_i T_y + \sum_{i=1}^n \omega_i x_i z_i R_x - \sum_{i=1}^n \omega_i (x_i^2 + y_i^2) R_z + \sum_{i=1}^n \omega_i y_i z_i R_y &= \sum_{i=1}^n \omega_i dx_i y_i - \sum_{i=1}^n \omega_i dy_i x_i. \end{aligned} \quad (17)$$

which simplifies to

$$[T_x, T_y, T_z, R_x, R_y, R_z]^T = \mathbf{H}^{-1} \mathbf{P}. \quad (18)$$

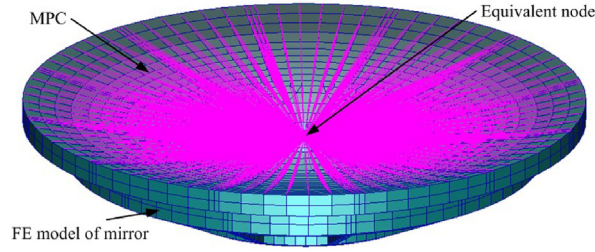


Fig. 18. Equivalent node representation of the mirror.

yielding a compact expression for the rigid-body displacement of the mirror. The matrix  $\mathbf{H}^{-1}\mathbf{P}$  can be expressed by the explicit-type multipoint constraint (MPC) in MSC Nastran [33]. In this manner, the equivalent node is used to represent the rigid-body displacement of the mirror (Fig. 18).

The assumptions applied to the space telescope are it being in-orbit and subject to small vibration amplitudes of its optical components. Hence, the response of the optical system can be treated linearly. By means of the optical design software, a correlation matrix of the mirror rigid body displacements and the motion of the image point on the image plane can be obtained. Specifically, the optical sensitivity coefficients matrix  $[L]_{img}$  and the equivalent displacements calculated above can be used to derive the displacement of the image point on image plane [34].

$$\begin{Bmatrix} \Delta x \\ \Delta y \end{Bmatrix} = [L]_{img} [T]_{optics} \tag{19}$$

The LOS of space telescope, denoted  $\theta_{obj}$  (Fig. 19) can then be calculated using the motion of the image point above [33],

$$\theta_{obj} = \frac{\Delta_{image}}{f_{eff}} \tag{20}$$

where  $\Delta_{image}$  is the image point motion and  $f_{eff}$  the equivalent focal length of the optical system.

The optical model established above needs to be verified (Fig. 20). The verification is divided into a) translation verification referring to a translation of the whole optical system (in theory, there should be no change in the angle of the optical axis) and b) rotation verification meaning that the LOS calculated using Eq. (20) should equal the rotation angle when the optical system is rotated as a whole.

4.1.3. Disturbance source model

The main micro-vibration sources of the space telescope dealt with are the momentum wheels in the telescope platform. In the FE model, the momentum wheels are concentrated mass points. The telescope platform includes three momentum wheels, and the disturbance data of a single momentum wheel is obtained from actual measurements. The test system (Fig. 21) includes a micro-vibration measurement platform [35].

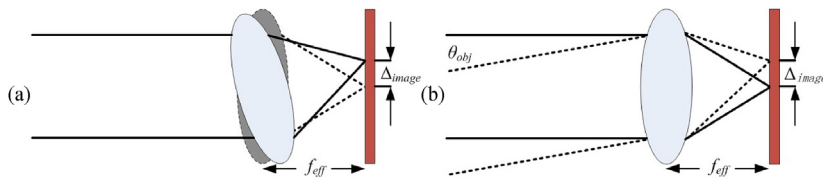


Fig. 19. Schematic diagram of the LOS: (a) real situation and (b) equivalent LOS.

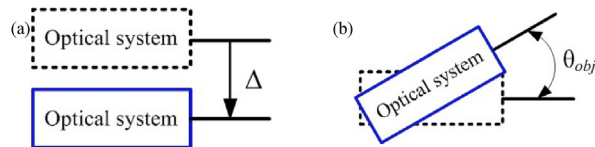


Fig. 20. Verification of the optical model: (a) in translation  $\theta_{obj} = 0$  and (b) in rotation  $\theta_{obj} = \frac{\Delta_{image}}{f_{eff}}$ .

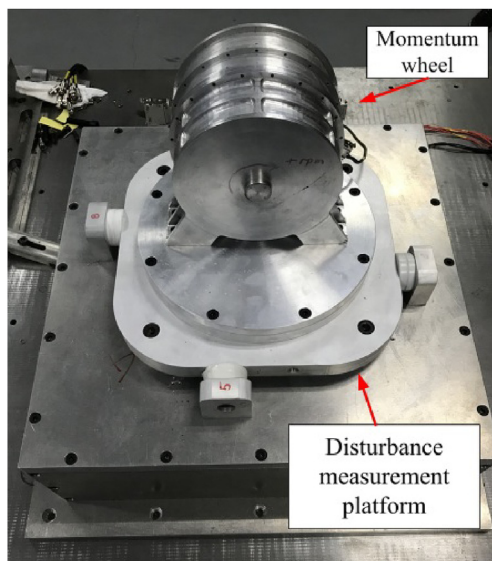


Fig. 21. Test system of a momentum wheel.

The test data (Fig. 22) are plotted as disturbance amplitudes of the momentum wheel against wheel rotation speeds for different frequencies. In the spectrum of the X-component of force [Fig. 22(a)], the main disturbance curves are marked. The most important disturbance frequencies in the low frequency range are the natural frequencies corresponding to the rotation speeds of the wheel. The main reason for these disturbances is an unbalanced rotor. In the high frequency range, there are V-shape curves, corresponding to the rocking whirl mode frequencies of the momentum wheel. The biggest disturbances appear at 2000 rpm, which is taken as an input for the simulations.

#### 4.2. Effect simulation of configuration optimization of the VIS

To verify the effect of configuration optimization of the VIS, we simulated two states of the space telescope: VIS with configuration optimization (as in Section 3.1) and VIS with cubic configuration (the parameters are shown in Section 3.1). Adopting the harshest condition when the three momentum wheels work together, a unit force/moment from the momentum wheel is applied at the mounting positions of the telescope platform, the kind of the excitation is a sine sweep. The LOS of the space telescope is calculated with these conditions, the curves for which are shown in Fig. 23. The frequency bandwidth of the integral modes of the VIS with configuration optimization is narrower than the cubic configuration. Moreover, its peak values have decreased slightly. That means the configuration optimization in Section 3.1 is effective.

#### 4.3. Effect simulation of stiffness optimization of the isolators

Assuming the configuration of the VIS has been determined, its configuration is the same as the optimized one in Section 3.1. To verify the effect of the stiffness optimization of each isolator, we simulated three states of the space telescope: without VIS, VIS without stiffness optimization (each isolator only has axial stiffness, as in Section 3.1) and VIS with stiffness optimization (each isolator has three different stiffness, as given in Section 3.2). The LOS of the space telescope is calculated with these conditions, the curves for which are shown in Fig. 24. Each curve can be divided into three zones corresponding to the integral mode, vibration attenuation, and local mode. In the integral mode zone, due to the installation of the VIS, resonance peaks are generated, corresponding to the integral modes. In this zone, the frequency bandwidth of the integral modes of the VIS with stiffness optimization is narrower than the other two states. Moreover, its peak values have decreased slightly. In the vibration attenuation zone, as the frequency bandwidth of integral modes is reduced, the curve corresponding to the VIS with stiffness optimization is below the other two states, implying that vibration isolation effect has improved. In the local mode zone, there are very dense peaks of three curves. These high-frequency resonance peaks arise from the vibrations of local components, such as the mirrors. In this zone, the curve of the VIS with stiffness optimization is located below that of no VIS, indicating that at high frequencies vibration isolation is active, and the VIS with stiffness optimization is effective.

To further illustrate the impact of VIS on the space telescope, the test data of the momentum wheel is imported into the micro-vibration integrated analysis model. The curves of the space telescope without VIS, with VIS without stiffness optimization, and with VIS with stiffness optimization (Fig. 25) show that with the presence of disturbance noise, the three curves all have dense peaks from 1 Hz to 300 Hz. The curve of VIS with stiffness optimization is always below the other two curves in the medium and high-frequency range. These results show that this state of VIS is effective. In addition, there are some high

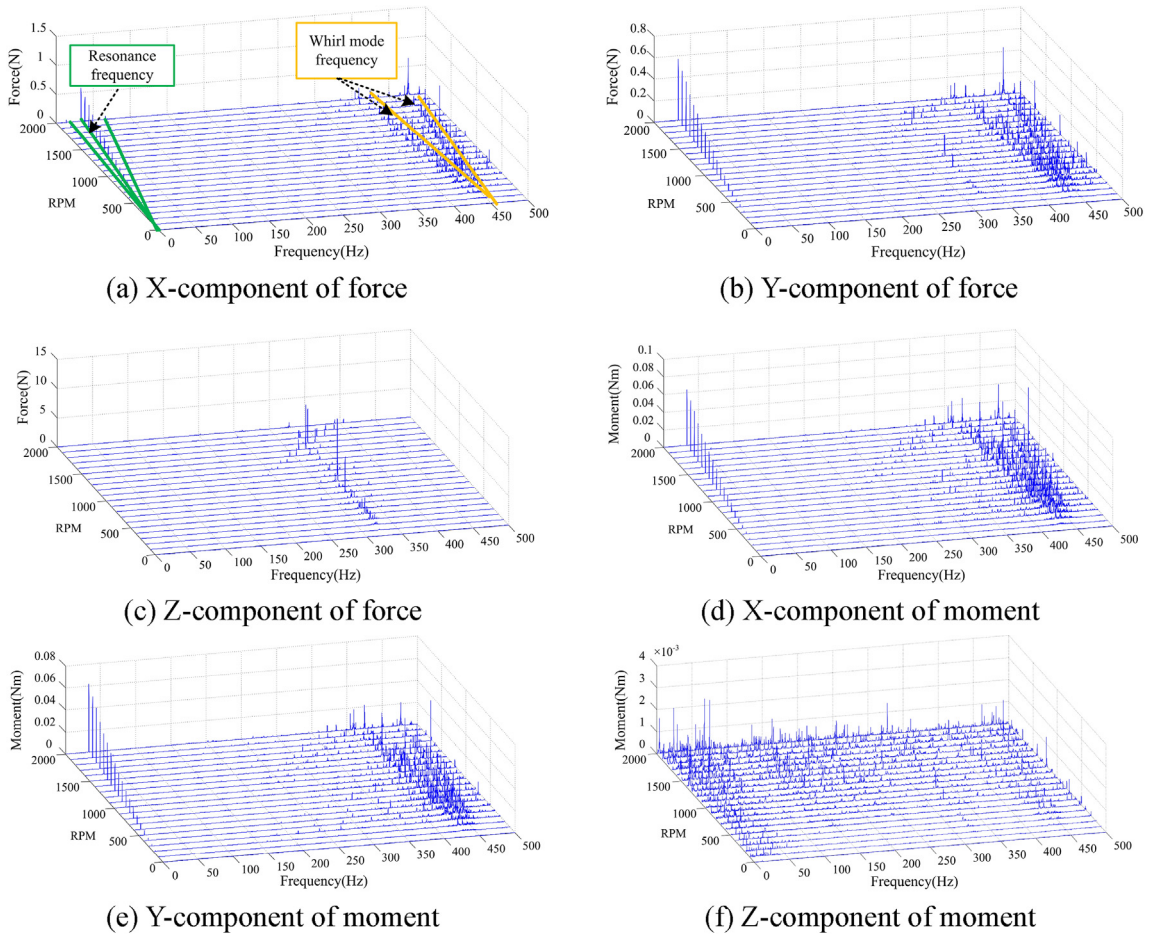


Fig. 22. Disturbance test results of the momentum wheel.

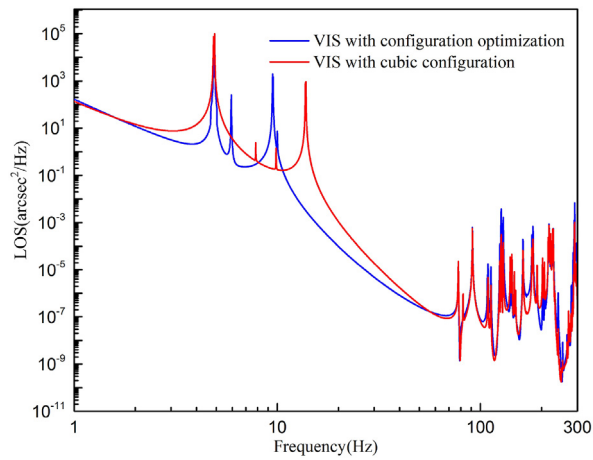


Fig. 23. Effect of configuration optimization of the VIS with a unit force/moment applied to the momentum wheels.

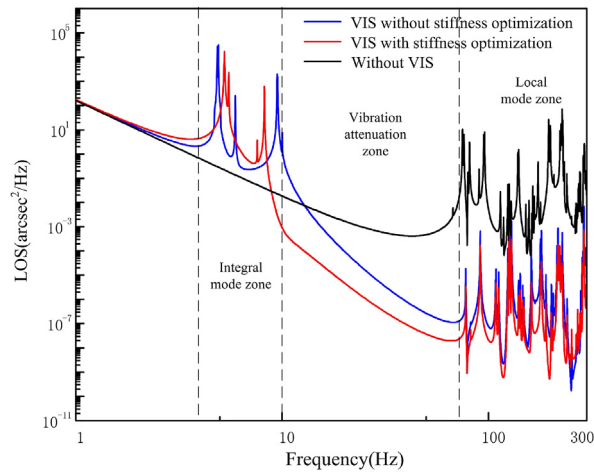


Fig. 24. Effect of stiffness optimization of the VIS with a unit force/moment applied to the momentum wheels.

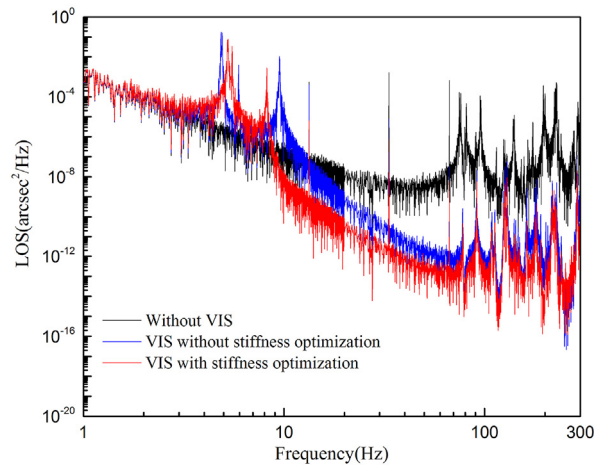


Fig. 25. LOS of the telescope with test data of the momentum wheels.

peaks at single frequencies. They are the main disturbance frequencies of the momentum wheels where the VIS with stiffness optimization also performs well.

The curves in Figs. 24 and 25 all have resonance peaks corresponding to the integral modes from 1 Hz to 10 Hz. In addition, the RMS of LOS in the frequency range 1–10 Hz was calculated (see Table 10). We find that the VIS leads to an amplification of the response indicating the need for damping for the VIS. In the next section, a method is described that resolves this problem.

#### 4.4. Simulations of the effect of damping

Inputting disturbances of one unit of force/moment from the momentum wheels, the LOS for the space telescope with VIS with stiffness optimization and with damping was calculated (Fig. 26).

In the high damping zone, because of damping, the peaks clearly weaken, and the curve becomes smoother. It shows that the installation mode of the dampers is effective. This also indicates that the layout of the dampers should be designed

**Table 10**  
RMS of LOS in 1–10 Hz.

State of VIS	RMS of LOS in 1–10 Hz ( $3\sigma$ )
Without VIS	0.056''
VIS without stiffness optimization and with damping	0.254''
VIS with stiffness optimization and damping	0.198''

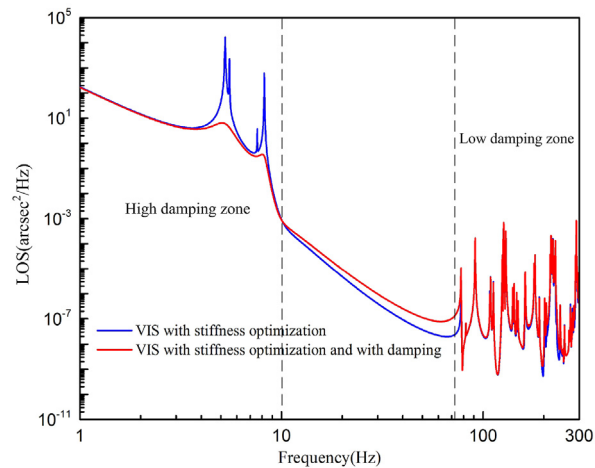


Fig. 26. Effect of damping of the VIS with stiffness optimization.

according to the installation mode of the isolators, and they are related. In the low damping zone, because of the characteristics of the viscous fluid dampers, the damping is smaller, and the shape of the curve changes a little. This behavior is more advantageous for the VIS in the high frequency range, because if the damping is large then a reduction in the effectiveness of VIS results in theory.

Furthermore, the LOS of the space telescope in the three states: without VIS, with VIS without stiffness optimization and with damping, and with VIS with stiffness optimization and with damping are calculated by applying the unit forces/moments of the momentum wheels. From the curves (Fig. 27), the resonance peaks in the integral mode zone decrease because of damping, and the curve of the VIS with optimization is smoother. In the vibration attenuation zone, the vibration attenuation is still obvious and the effect of the VIS with stiffness optimization is still the best. In the local mode zone, because damping decreases in the high-frequency range, the relative position of the three curves is not different from the state without damping.

#### 4.5. Effect of comprehensive vibration isolation measures

Finally, applying the test data of the momentum wheels, the LOS of the space telescope with all vibration isolation measures included was calculated (Fig. 28). In the low-frequency range, the curve of the VIS with stiffness optimization and with damping is smoother, and the frequency bandwidth of the integral modes of this state is narrower than the other two states. When frequencies are above 10 Hz, the curve of the VIS with stiffness optimization and with damping is always below the others, indicating the vibration isolation is the most effective. At the main disturbance frequencies of the momentum wheels, its effectiveness is still better than the others. In addition, the RMS of the LOS was calculated (Table 11). Compared

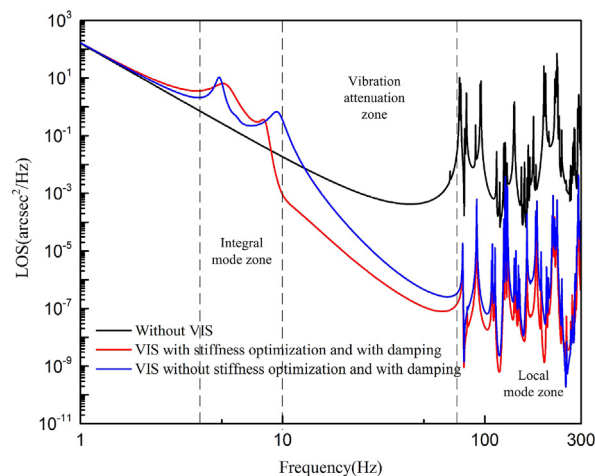


Fig. 27. Comparison of a VIS with damping but without stiffness optimization and a VIS with damping and with stiffness optimization.

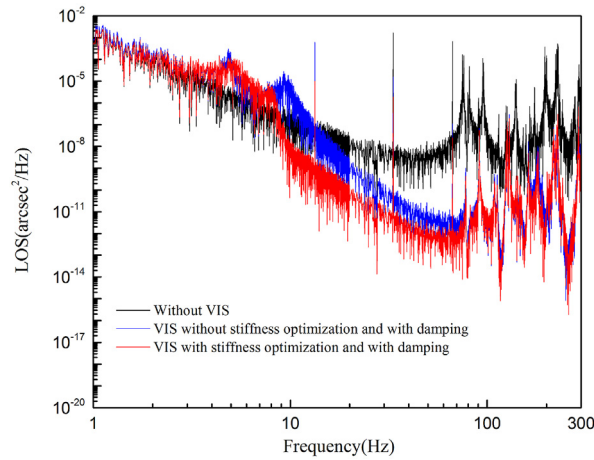


Fig. 28. Effect of comprehensive vibration isolation measures.

**Table 11**  
RMS of LOS of the three states.

State of VIS	RMS of LOS ( $3\sigma$ )
Without VIS	0.127"
VIS without stiffness optimization and with damping	0.091"
VIS with stiffness optimization and damping	0.066"

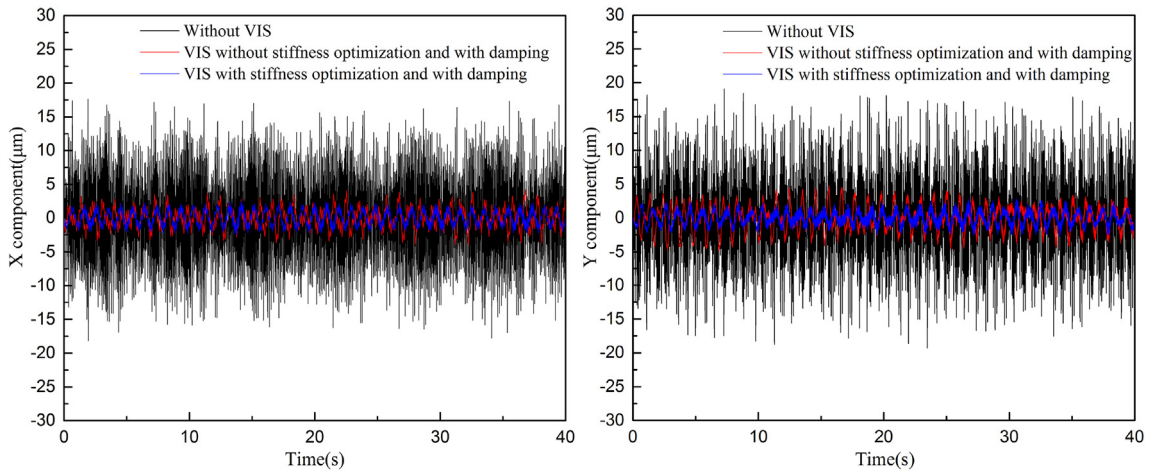


Fig. 29. Displacement of image point in time domain.

with the state of the telescope without VIS, the RMS is attenuated by 48%. With the VIS with stiffness optimization and with damping, the effectiveness is obvious.

A time domain analysis was also conducted in regard to the displacement of the image point on the image plane (Fig. 29). The results show the displacement of the image point decreasing quite clearly for a VIS with stiffness optimization and with damping. In addition, because of the asymmetric structure of the space telescope and the asymmetric locations of the disturbance sources, the attenuation of the Y component is more obvious.

In addition to understanding more clearly the change in position of an image point on the image plane, the position of the image point on the image plane over a time interval was simulated (Fig. 30). The positions of the image point are more concentrated with a VIS with stiffness optimization and damping.

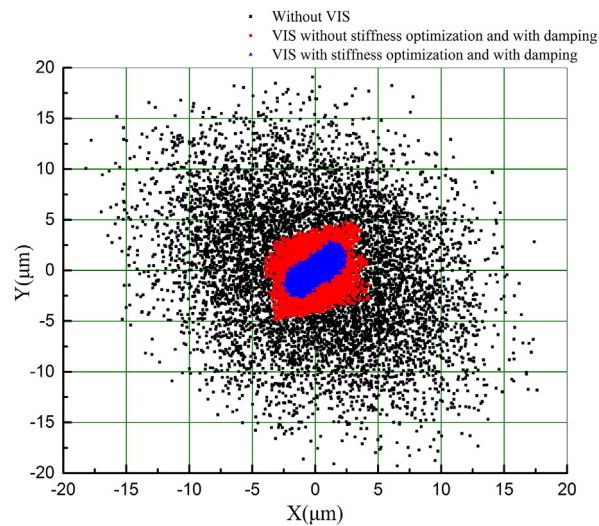


Fig. 30. Positions of the image point on the image plane at different times.

## 5. Conclusions

The micro-vibration isolation technology of large space telescope has been studied in this paper. A method of design and optimization of the VIS for optical payload was proposed. For improving the vibration attenuation effect of the VIS, the configuration of the VIS, and the stiffness and damping of a single vibration isolator were considered synthetically in the method. The integrated analysis results in both frequency and time domain show that: compared with the space telescope without VIS, the attenuation rate of LOS is 48%, and the displacement of the image point are more centralized by applying this method. All the results above demonstrate that the VIS designed in this study reduced effectively the influence of the micro-vibration sources of the telescope platform on the space telescope.

## Declaration of competing interest

The authors declare that they have no known competing financial interests or personal relationships that could have appeared to influence the work reported in this paper.

## CRedit authorship contribution statement

**Chao Qin:** Conceptualization, Methodology, Writing - original draft, Formal analysis, Validation. **Zhenbang Xu:** Conceptualization, Supervision. **Mingyi Xia:** Validation. **Shuai He:** Formal analysis. **Jingxu Zhang:** Software, Investigation.

## Acknowledgements

This work is supported by the National Natural Science Foundation of China [grant number 11672290]; National Key R&D Program of China [grant number 2016YFE0205000]; This work is supported by the National Natural Science Foundation of China [grant number 91848202].

## Appendix A. Supplementary data

Supplementary data to this article can be found online at <https://doi.org/10.1016/j.jsv.2020.115461>.

## References

- [1] M. Toyoshima, Y. Takayama, H. Kunimori, In-orbit measurements of spacecraft micro-vibrations for satellite laser communication links, *Opt. Eng.* 49 (8) (2010) 1–10.
- [2] G.S. Aglietti, R.S. Langley, E. Rogers, S.B. Gabriel, Model building and verification for active control of microvibrations with probabilistic assessment of the effects of uncertainties, *Proc. Inst. Mech. Eng. Part C-J. Eng. Mech. Eng. Sci.* 218 (4) (2004) 389–399.
- [3] Quan Hu, Yinghong Jia, Shijie Xu, Adaptive suppression of linear structural vibration using control moment gyroscopes, *J. Guid. Contr. Dynam.* 37 (3) (2014) 990–996.
- [4] N. Jedrich, D. Zimbelman, M. Turczyn, J. Sills, C. Voorhees, B. Clapp, Cryocooler induced micro-vibration disturbances to the hubble space telescope, in: *Proceedings of Cranfield Space Dynamics Conference, 2002*, pp. 1–7.
- [5] R. Ullio, F. Marta, Artemis micro-vibration environment prediction, *Proc. Eur. Conf. Spacecraft Struct. Mater. Mech. Test.* (1999) 489–495.

- [6] Q. Luo, D. Li, W. Zhou, J. Jiang, G. Yang, X. Wei, Dynamic modelling and observation of micro-vibrations generated by a single gimbal control moment gyro, *J. Sound Vib.* 332 (19) (2013) 4496–4516.
- [7] Li Lin, Luyang Tan, Lin Kong, Dong Wang, Hongbo Yang, The influence of flywheel micro vibration on space camera and vibration suppression, *Mech. Syst. Signal Process.* 100 (2018) 360–370.
- [8] Qing Luo, Dongxu Li, Jianping Jiang, Analysis and optimization of microvibration isolation for multiple flywheel systems of spacecraft, *AIAA J.* 54 (5) (2016) 1719–1731.
- [9] Chunchuan Liu, Xingjian Jing, Steve Daley, Fengming Li, Recent advances in micro-vibration isolation, *Mech. Syst. Signal Process.* 56 (2016) 55–80.
- [10] D. Kamesh, R. Pandiyan, A. Ghosal, Passive vibration isolation of reaction wheel disturbances using a low frequency flexible space platform, *J. Sound Vib.* 331 (6) (2012) 1310–1330.
- [11] Dr Vanessa Camelo, Dr Allen Bronowicki, Dr Stepan Simonian, Dr Reem Hejal, Dr Sarah Brennan, Damping and isolation concepts for vibration suppression and pointing performance, in: 50th AIAA/ASME/ASCE/AHS/ASC Structures, Structural Dynamics, and Materials Conference, Palm Springs, 2009, pp. 1–16.
- [12] Allen J. Bronowicki, Vibration isolator for large space telescopes, in: 45th AIAA/ASME/ASCE/AHS/ASC Structures, Structural Dynamics, and Materials Conference, Palm Springs, 2004, pp. 1–13.
- [13] Kuo-Chia Liu, Carl Blaurock, Gary E. Mosier, Pointing control system design and performance evaluation of TPF coronagraph, *Model. Syst. Eng. Astron.* 5497 (2004) 437–449.
- [14] William R. Oegerle, Lee D. Feinberg, Lloyd R. Purves, et al., ATLAST-9.2m: a large-aperture deployable space telescope, *SPIE* 7731 (2010) pp. 1–10, 77312M.
- [15] Allen J. Bronowicki, John W. Innis, A family of full spacecraft-to-payload Isolators, *Technol. Rev. J* 13 (2005) 21–41.
- [16] Hong-Jen Chen, Ronald M. Bishop Jr., Brij N. Agrawal, Payload pointing and active vibration isolation using hexapod platforms, in: 44th AIAA/ASME/ASCE/AHS/ASC Structures, Structural Dynamics, and Materials Conference, Norfolk, 2003, pp. 1–19.
- [17] M. Brett McMickell, Thom Kreider, Eric Hansen, Torey Davis, Mario Gonzalez, Optical payload isolation using the miniature vibration isolation system (MVIS-II), in: *SPIE*, vol. 6527, 2007, pp. 1–13, 652703.
- [18] Doug Thayer, Mark Campbell, Juris Vagners, Six-axis vibration isolation system using soft actuators and multiple sensors, *J. Spacecraft Rockets* 39 (2) (2002) 206–212.
- [19] Yao Zhang, Shijie Xu, Vibration isolation platform for control moment gyroscopes on satellites, *J. Aero. Eng.* 25 (4) (2011) 641–652.
- [20] Jianfeng Yang, Zhenbang Xu, Qingwen Wu, Zhongsu Wang, Hang Li, Shuai He, Design of a vibration isolation system for the space telescope, *J. Guid. Contr. Dynam.* 38 (12) (2015) 2441–2448.
- [21] Keith B. Doyle, Design optimization of a dual mode multi-axis passive isolation configuration for MLCD, in: *SPIE*, vol. 6665, 2007, pp. 1–12, 66650G.
- [22] Wei-Yong Zhou, Dong-Xu Li, Qing Luo, Jian-Ping Jiang, Design and test of a soft suspension system for cantilevered momentum wheel assembly, *Proc. Inst. Mech. Eng. Part G-J. Aerosp. Eng.* 227 (7) (2013) 1144–1160.
- [23] Mattias Sjöberg, Leif Kari, Non-linear behavior of a rubber isolator system using fractional derivatives, *Veh. Syst. Dyn.* 37 (3) (2002) 217–236.
- [24] P. Davis, D. Cunningham, J. Harrell, Advanced 1.5 Hz passive viscous isolation system, in: Presented at the 35th AIAA SDM Conference Hilton Head, South Carolina, 1994, pp. 1–11.
- [25] Porter Davis, David Cunningham, Adaptable passive viscous damper (an adaptable D-Strut™), in: *SPIE*, vol. 2193, 1994, pp. 47–59.
- [26] P. Davis, D. Cunningham, T.T. Hyde, Second-generation hybrid D-strut, in: Proceedings of the SPIE Smart Structures and Materials Conference, San Diego, CA, February 1995, pp. 1–15.
- [27] H.U. Oh, Experimental demonstration of an improved magneto-rheological fluid damper for suppression of vibration of a space flexible structure, *Smart Mater. Struct.* 13 (5) (2004) 1238–1244.
- [28] Kuo-Chia Liu, Thomas Kenney, Peiman Maghami, Pete mule, jitter test program and on-orbit mitigation strategies for solar dynamic observatory, in: Proceedings of the 20th International Symposium on Space Flight Dynamics, vol. 214158, NASA Technical Reports, 2007.
- [29] David W. Miller, Olivier L. de Week, Gary E. Mosier, Framework for multidisciplinary integrated modeling and analysis of space telescopes, in: *SPIE*, vol. 4757, 2002, pp. 1–18.
- [30] John D. Johnston, Joseph M. Howard, Gary E. Mosier, Keith A. Parrish, et al., Integrated modeling activities for the James Webb space telescope structural-thermal-optical analysis, in: *SPIE*, vol. 5487, 2004, pp. 600–610.
- [31] Hyun-Ung Oh, Katsuhiko Izawa, Shigemune Taniwaki, Development of variable-damping isolator using bio-metal fiber for reaction wheel vibration isolation, *Smart Mater. Struct.* 14 (5) (2005) 928–933.
- [32] Jim Boyd, T. Tupper Hyde, Dave Osterberg, Torey Davis, Performance of a launch and on-orbit isolator, in: *SPIE*, vol. 4327, 2001, pp. 433–440.
- [33] K.B. Doyle, V.L. Genberg, G.J. Michels, Integrated Optomechanical Analysis, SPIE Publ, Bellingham, 2000.
- [34] Victor L. Genberg, Keith B. Doyle, Gregory J. Michels, Optical performance as a function dynamic mechanical loading, in: *SPIE*, vol. 5178, 2004, pp. 14–20.
- [35] Mingyi Xia, Zhenbang Xu, Kang Han, Huo Qi, Ang Li, Dynamic disturbance force measurement platform for large moving device in spacecraft, *J. Sound Vib.* 447 (2019) 61–67.